Plastic Instability during Creep Deformation of a NiAl-Hf Single-Crystal Alloy—A Case Study

A. GARG, S.V. RAJ, R.D. NOEBE, M.V. NATHAL, and R. DAROLIA

Tensile samples from NiAl-Hf single crystals, having the same nominal composition and heat treated and creep tested under identical conditions at 1144 K, were found to exhibit very different rupture lives and creep ductilities. A case study was conducted on two samples with creep rupture lives of 343.6 and 37.0 hours (with corresponding creep ductilities of 12.3 and 39.9 pct, respectively) in order to find the causes of such a large variation in creep properties. Detailed microstructural analyses using optical microscopy, scanning electron microscopy (SEM), and transmission electron microscopy (TEM) indicated that the sample with higher rupture life and lower ductility had deformed uniformly along the length of the gage section, whereas the sample with lower rupture life and higher ductility (sample L) deformed by localized plastic deformation resulting in shear failure. This shear failure was due to a plastic instability in sample L which was caused by the presence of a high density of large Hf-rich interdendritic particles that were formed during casting of the single-crystal ingot but did not go into solution during the homogenization heat treatment. The role of these particles in causing nonuniform deformation, which led to strain localization and a premature failure in sample L, has been described in detail.

I. INTRODUCTION

THE service life of structural materials is severely affected by nonuniform deformation and localized plasticity, which often lead to a premature failure.[1] Depending on the circumstances, both the material's plastic flow response and explicit strain softening processes, either alone or in combination, can lead to the development of a plastic instability. The study of plastic flow localization is important since it provides a connection between defect properties of the material and bulk deformation behavior on a macroscopic scale. On a microscopic level, it helps to identify the critical conditions that lead to the cooperative dislocation phenomenon responsible for the evolution of a localized flow pattern during plastic deformation. In either case, a better understanding of the localization phenomena at the defect scale is highly desirable, especially in ''new'' material systems where development and progress can be hindered without the knowledge of such an understanding.

Intermetallic compounds and their alloys are being developed as the next generation of high-temperature structural materials for more efficient civil transport systems for the twenty-first century. NiAl-based alloys have proven to be one of the more promising intermetallic candidates, since they possess a desirable combination of properties which are significantly superior to those of the currently used commercial superalloys.[2,3] However, two limitations that have historically prevented the use of NiAl in advanced turbine engines are its low ductility at ambient temperatures and poor creep strength at high temperatures. In recent years, significant alloy development effort has gone into producing creep-resistant NiAl single crystals containing minor alloying additions, and there is now considerable data which suggest that the desired creep strength levels can be achieved in NiAl single crystals alloyed with Hf and other reactive and refractory elements.[4–7]

However, no new alloy development effort is free from problems, and understanding the causes of these problems and finding their practical solutions is critical to the success of any alloy development program. One of the obstacles encountered in the development of NiAl-Hf single-crystal alloys was the observation of an unacceptable amount of scatter among different samples machined from various ingots of the same alloy composition. In order to understand why samples of the same nominal composition, given the same heat treatment and creep tested under identical conditions, were deforming differently, two samples with the lowest and the highest creep life were chosen from a batch of creep-tested samples[8] for a detailed examination using optical microscopy scanning electron microscopy (SEM), and transmission electron microscopy (TEM). Analysis of the data indicated that the variation in the creep-rupture lives of these two samples was related to a plastic instability that developed in the low-life sample. This plastic instability manifested itself in the development and growth of macroscopic shear bands, which resulted in a localized shear failure. The cause of this plastic instability and the microprocesses that led to strain softening and slip localization are described in this article.

II. EXPERIMENTAL

Single-crystal ingots of nominal composition NiAl-0.5Hf (at. pct) were grown from the melt by a modified Bridgman technique at General Electric Aircraft Engines (GEAE) (Cincinnati, OH). The homogenization heat treatment of the ingots consisted of solution treating at 1590 K for 50 hours in a flowing argon atmosphere followed by furnace cooling.

A. GARG, Material Research Engineer, is with AYT Corp. working at NASA-Lewis Research Center, Cleveland,, OH 44135. S.V. RAJ, and R.D. NOEBE, Materials Research Engineers, and M.V. NATHAL, Branch Chief, are with the Advanced Metallics Branch, NASA–Lewis Research Center, Cleveland, OH 44135. R. DAROLIA, Principal Engineer, is with General Electric Aircraft Engines, Cincinnati, OH 45215.

Manuscript submitted April 28, 1997.

Table I. Tensile Creep Rupture Data for a [001] NiAl(Hf) Single-Crystal Alloy*

Specimen ID (Ingot-sample Number)	Deviation from [001] Axis	Creep Ductility ε_f (Pct)	Rupture Life t_f (h)
A-8 (L)	≤1.0 deg	39.9	37.0
A-11	2.0 deg	34.2	49.1
C-5	1.5 deg	29.8	173.4
D-16	≤1.0 deg	11.0	322.5
B-17 (H)	1.5 deg	12.3	343.6

Creep stress: 241.4 MPa.
Temperature 1144 K.

Table II. Chemical Composition of the Specimens* (Atomic Percent)

Specimen	Ni	Al	Hf	Cr	Si	Fe
Low life (L)	50.1	48.5	0.46	0.47	0.23	0.27
High life (H)	49.9	48.6	0.52	0.47	0.20	0.29

*The error in the measurement is ~5 pct.

Higher solution heat-treatment temperatures were preferred but avoided, since they often resulted in local incipient melting of the alloy. Homogenization of the ingots was performed in batches, where each batch typically consisted of five to ten ingots. Cylindrical buttonhead specimens for stress rupture testing along ⟨001⟩ were machined from different ingots. Constant-load stress rupture testing was conducted in air at 1144 K under an initial stress of 241.4 MPa by Joilet Metallurgical Laboratories Inc. (Joilet, IL) for GEAE. Although the exact form of the strain-time curves was not available, the test data indicated a wide variation in creep properties, with creep rupture life (t_f) varying from 37 to 343.6 hours and creep ductility (ε_f) varying from 39.9 to 12.3 pct. This is shown in Table I for a batch of five specimens. Such a large variation is obviously not acceptable; thus, post-test optical/SEM examination was conducted on all the specimens and, thereafter, two specimens with the extreme values of t_f were chosen for detailed TEM analysis. These two specimens, with specimen IDs A-8 and B-17 and t_f:ε_f of (37 hours:39.9 pct) and (343.6 hours:12.3 pct), are abbreviated as specimens L and H, respectively, according to their low and high creep life. It should be noted that these two specimens were machined from two different ingots, designated as A and B in the specimen ID column in Table I.

One half of each of the two stress-rupture specimens was available and used for detailed examination and analysis. Therefore, care was taken to obtain maximum information from the as-fractured specimens before using any destructive technique. First, the morphology of the fractured specimens, shapes of the fracture surfaces, and slip traces on the sample surfaces were documented. Second, the fracture surfaces of the failed specimens were examined in a JEOL*-840 SEM equipped with a KEVEX** X-ray detector. Energy dispersive spectroscopy (EDS) and X-ray mapping were utilized to obtain chemical information when necessary. The X-ray Laue diffraction technique was used to double-check the orientation of each specimen in the buttonhead region. Having obtained these pieces of information, the specimens were mounted, ground, and polished longitudinally to their midsections (approximately) for optical examination. The microstructures of the gage and buttonhead sections in each sample were examined in the as-polished condition and also after etching. The etchant used was a freshly prepared solution of 33 pct nitric acid, 33 pct acetic acid, 1 pct hydrofluoric acid, and 33 pct water. Chemical analysis of the samples was also performed to verify the composition of each sample, which is given in Table II.

Detailed TEM analysis was conducted on the specimens using a PHILIPS* 400T TEM. Electrochemically polished foils for TEM were prepared from the ground longitudinal sections of the specimens after optical examination. The electrolyte used was a solution of 70 pct ethanol, 14 pct distilled water, 10 pct butylcellosolve, and 6 pct perchloric acid cooled to 263 K. An applied potential of 20 to 25 V with a corresponding current of 10 to 15 mA produced electron-transparent foils. The TEM foils were prepared from different regions of the gage section and from the buttonhead section. The buttonhead sections were examined to compare the unstressed regions and the effect of temperature on the microstructures of the two specimens. Due to the geometry of the ground specimens, the TEM samples from each region were made from the longitudinal section, such that the foil plane was approximately parallel to the loading axis.

*JEOL is a trademark of Japan Electron Optics Ltd., Tokyo.
**KEVEX is a trademark of Kevex Corporation, Foster City, CA.
*PHILIPS is a trademark of Philips Electronic Instruments Corp., Mahwah, NJ.

III. RESULTS

A. *Optical and SEM Study*

The cross-sectional shape of the gage near the fracture surfaces of the two specimens was observed to be distinctly different. The gage remained circular for sample H but became extremely elliptical during testing of sample L, as shown in Figures 1(a) and (b), respectively. The gage surfaces of the specimens were also examined for slip traces. Although the specimens were badly oxidized during creep testing, evidence of duplex slip could be seen on the surface of specimen H (Figure 1(c)), but any characteristic features that could be associated with slip traces on sample L were not uniquely identified.

An SEM examination of the fracture surfaces revealed a quasicleavage-type fracture behavior in specimen H (Figure 2(a)), whereas specimen L showed a mixture of elongated dimples (Figure 2(b)) and cleavage facets (Figure 2(c)). Porosity was occasionally observed in the specimens, but it did not appear to be the cause of the final failure in either sample. The X-ray Laue patterns obtained from the buttonhead regions of the specimens confirmed that the orientations were within ±2 deg of the desired ⟨001⟩ orientation (Table I), which is too small to cause any change in the slip system activation.

The metallographically polished longitudinal sections of the specimens were examined in an optical microscope to see if there were any macrostructural differences that could have influenced the creep properties. It was found that the

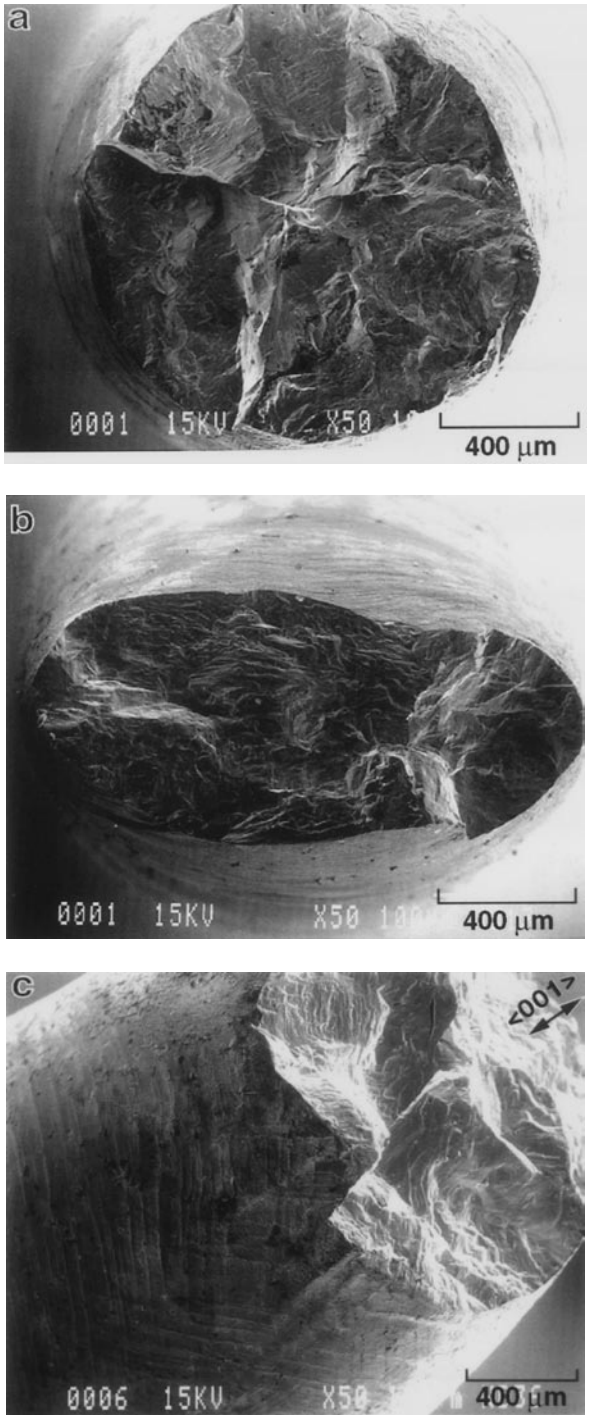

Fig. 1—Macroscopic view showing geometry of sample cross section after testing: (*a*) circular for specimen H and (*b*) elliptical for specimen L. (*c*) SEM micrograph showing duplex slip traces on the gage surface of specimen H.

low-life specimen (L) contained several interdendritic particles of size varying from 5 to 500 μm. Examination of the various sections of ingot A, from which the two low-life specimens were machined, showed that it contained a reasonably high density of large interdendritic particles, as shown in Figure 3(a). In contrast, the high-life specimen was almost free of such large particles and only occasionally showed the presence of small particles ≤1.0 μm in size

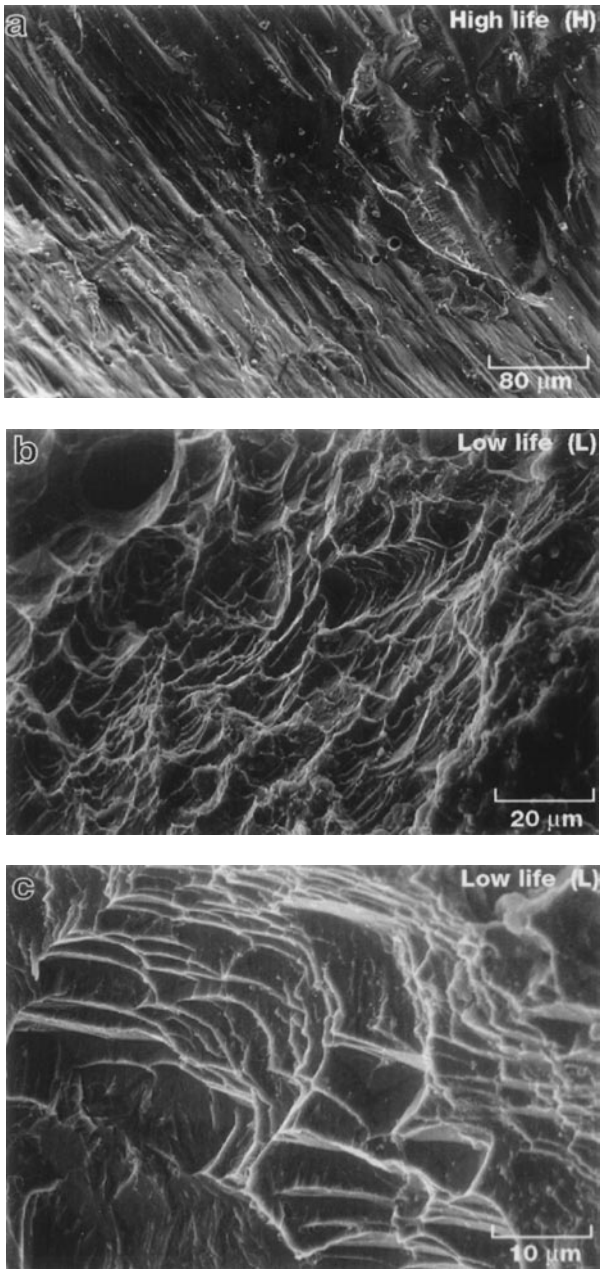

Fig. 2—SEM fractographs showing (*a*) cleavage facets in specimen H and (*b*) and (*c*) elongated dimples and cleavage facets in specimen L.

(arrowed); the worst-case scenario is shown in Figure 3(b). Our extensive experience with the other NiAl-Hf series alloys homogenized under similar conditions has shown that such undissolved interdendritic particles often exist in the Hf-containing NiAl single crystals, although their size and density may vary from one ingot to the other. A complete characterization of these particles was undertaken in a parallel study,[9] where it was found that each of the larger ''particles'' was actually a complex agglomeration of at least three phases. A backscatter electron image of a typical such particle is shown in Figure 4(a). A chemical analysis of the phases was obtained *via* EDS, which showed that the black phase (marked Y) contained only Ni and Al, whereas both the gray phase (marked X) and the bright phase (marked Z) showed enrichment of Hf. Since the gray

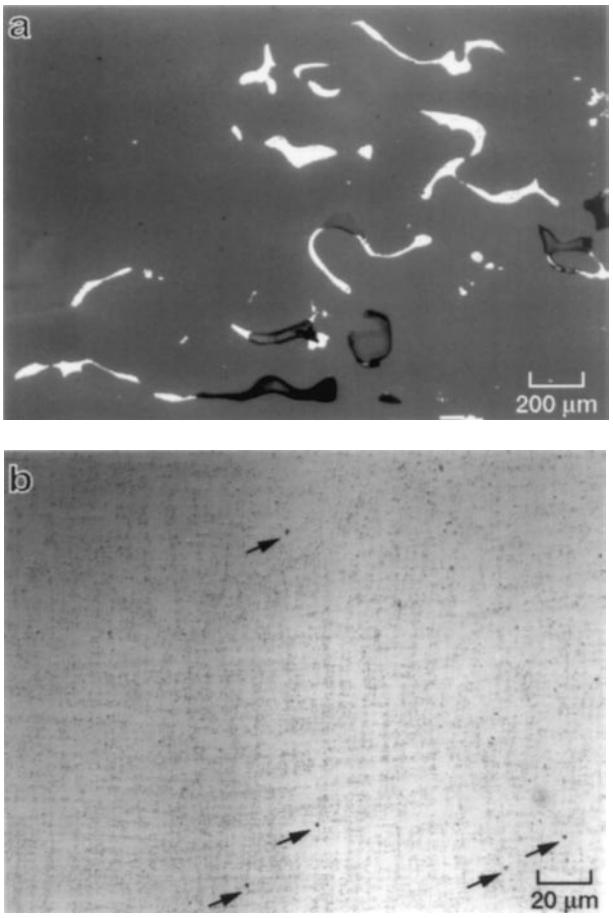

Fig. 3—Representative micrographs showing (*a*) a high density of large Hf-rich interdendritic particles in sample L and (*b*) a low density of small Hf-rich particles (arrowed) in sample H. Note the different magnifications in (a) and (b).

and white regions obviously correspond to two different phases, wavelength dispersive X-ray elemental mapping was undertaken, which showed that the bright regions also contained significant amounts of Si in addition to Hf (Figures 4(b) and (c)). The presence of Si was not unambiguously identified in the EDS due to proximity of the Si K_α (1.745 keV) and the Hf M_α (1.645 keV) energy peaks, which resulted in their overlap. Thus, the gray phase (X) was enriched in Hf, Ni, and Al, and was identified as the Heusler phase (Ni_2AlHf*). This phase was the primary phase in each particle and was also present in the three phase regions. The other two phases mainly present in the three phase regions were enriched in Ni and Al (Y), and Ni, Hf, and Si (Z), and these were identified as the NiAl and NiHfSi* phases, respectively. The smaller particles occasionally observed in sample H (Figure 3(b)) were predominantly the Heusler phase. It should be mentioned that Si is not intentionally added to the alloy, but is picked up from reaction with the ceramic alumina-silicate shell mold used for melting and casting of the single-crystal ingots. This results in the formation of various silicon-rich phases such as $Ni_{16}Hf_6Si_7$ (known as the G phase) and NiHfSi.[7,10,11]

*The crystal structure of these phases was confirmed by electron diffraction later in the TEM study.

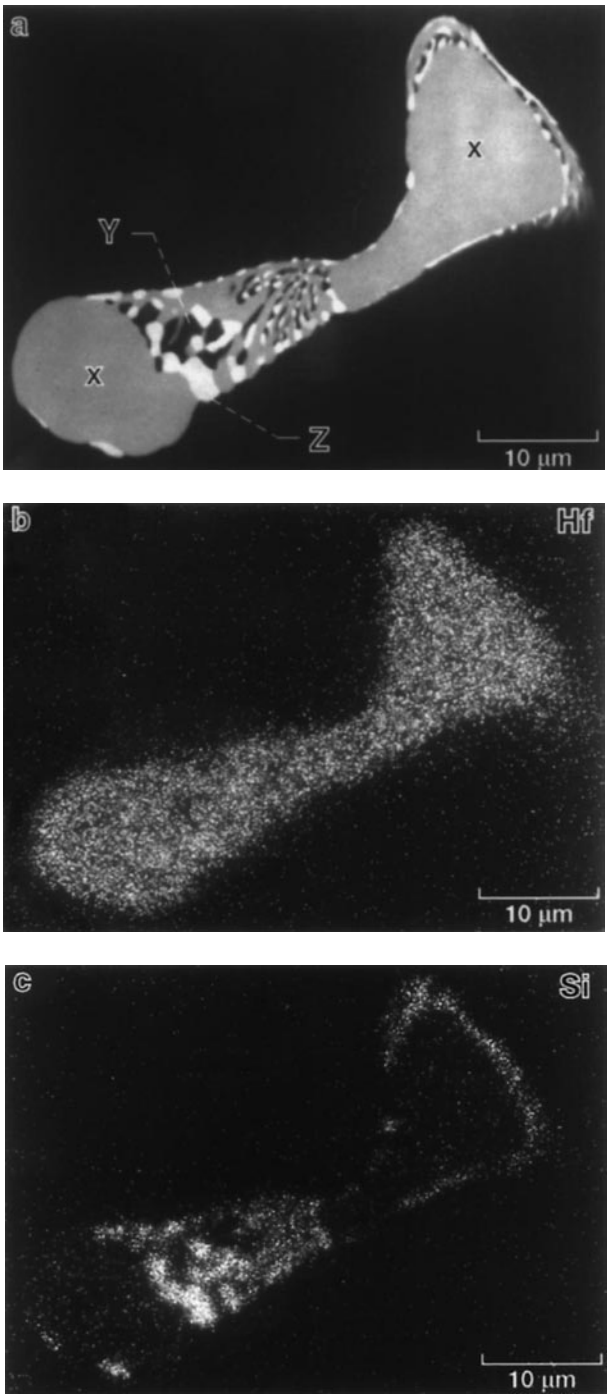

Fig. 4—(*a*) A BSE-SEM image showing the multiphase nature of a typical interdendritic particle observed in sample L. X-ray elemental maps show enrichment of (*b*) Hf and (*c*) Si in different regions of the particle.

B. *TEM Study*

Figures 3 and 4 provide a strong clue to the source of the difference in behavior of the two specimens. However, questions as to why the interdendritic particles would promote higher ductility or an elliptical cross section of the fracture surface prompted a more detailed study. Therefore, TEM was undertaken to examine and analyze the initial and deformed microstructures and, thus, to identify the mode of deformation in each of the two specimens. A general TEM microstructure of the buttonhead section of specimen L

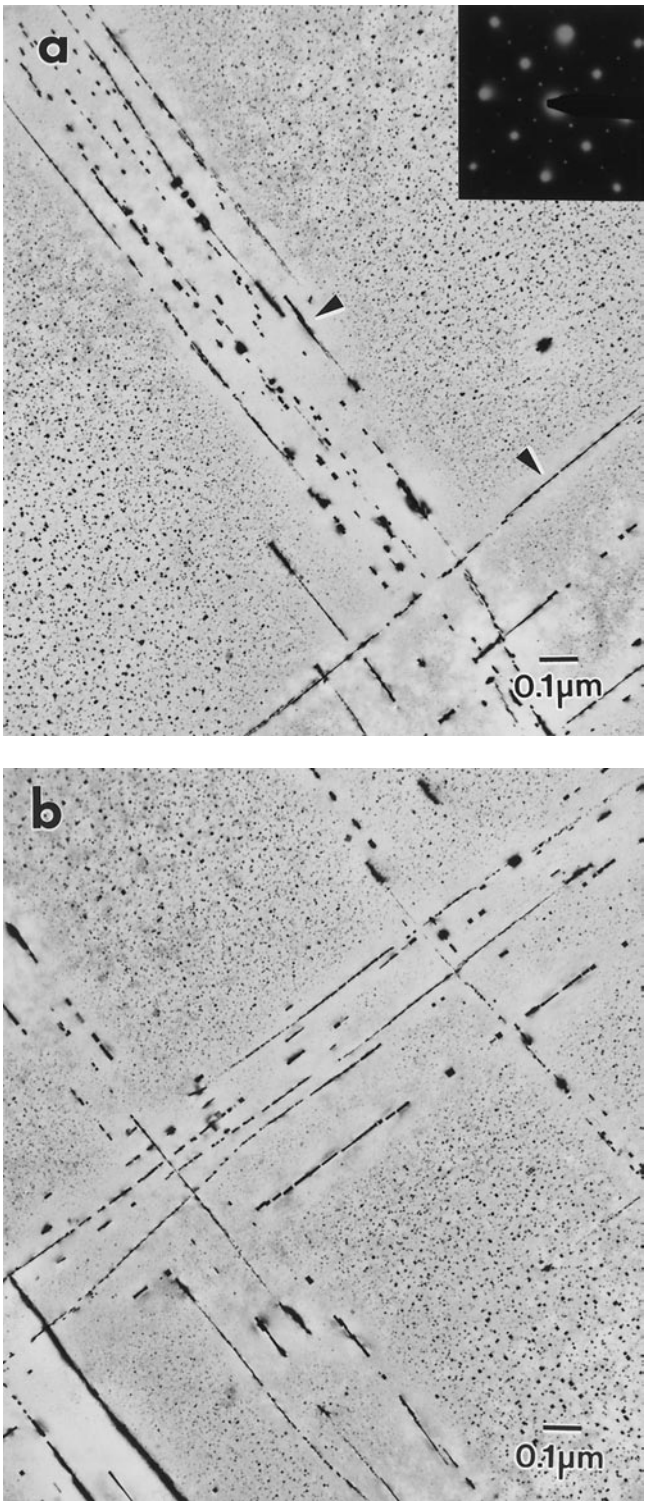

Fig. 5—TEM micrographs close to a ⟨001⟩ zone axis showing general microstructure in the buttonhead region of specimens (*a*) L and (*b*) H. The SADP in (a) shows a cube-on-cube orientation relationship between the G-phase precipitates and NiAl matrix.

close to a $\langle 100 \rangle_{NiAl}$ zone-axis is shown in Figure 5(a). The microstructure consisted of a high density of fine cuboidal precipitates (size ≈5 to 20 nm) which were distributed uniformly in the NiAl matrix, and some plate-shape precipitates (size ≈100 nm) on edge-on $\{010\}_{NiAl}$ planes resulting in a grid-type pattern (arrows in Figure 5(a)). A selected area diffraction pattern (SADP), shown in the top right-hand corner in Figure 5(a), showed a cube-on-cube orientation relationship between the precipitates and the matrix, and an fcc structure with lattice parameter $a_0 = 1.144$ nm for the precipitate phase. This phase was identified as the G phase ($Ni_{16}Hf_6Si_7$), which has been reported to precipitate in NiAl single crystals containing Hf and Si.[7] The G phase has a small misfit (1.2 pct) and nucleates coherently in the NiAl matrix ($a_0 = 0.289$ nm). Those precipitates which nucleate on dislocations grow at an accelerated rate, presumably due to a pipe diffusion mechanism, and adopt a plate-shape morphology resulting in minimization of strain energy. The G-phase platelets were associated with precipitate-free zones that can be clearly seen in Figure 5. The general microstructure of the buttonhead section of sample H (Figure 5(b)) was essentially identical to that of sample L (Figure 5(a)). Although the two samples were exposed to 1144 K for quite different times (37 hours for L *vs* 343.6 hours for H), no apparent differences in the size, distribution, and morphology of the G-phase precipitates in the two samples could be discerned. This suggested that the G phase was thermally stable and had slow coarsening kinetics at 1144 K.

In addition to the fine G-phase precipitates, larger Hf-rich particles were observed in the TEM foils made from the gage and buttonhead sections of both the specimens. Significantly, in specimen L several such particles were encountered in each foil, whereas in sample H, these particles were rare, and whenever observed had a much smaller (submicron) size. A representative micrograph showing some of these particles (marked by arrows) in the TEM foils of each of the two specimens is shown in Figures 6(a) and (b). These TEM observations are consistent with the optical observations reported in Figure 3. Frequently, the large Hf-rich particles fell out during electropolishing due to preferential thinning at the particle-matrix interface, leaving behind holes in the foil. This was a particular problem for foils made from specimen L. Occasionally, a part of the Hf-rich particle that was still attached to the matrix could be seen near the hole, and its edges were thin enough to obtain electron diffraction patterns. Microbeam electron diffraction patterns (MBED) were obtained from these particles, which were indexed to either the fcc Ni_2AlHf ($a = 0.608$ nm) structure or the orthorhombic NiHfSi ($a = 0.639$ nm, $b = 0.389$ nm and $c = 0.72$ nm) structure.[17,10–12] Typical diffraction patterns obtained from each of these phases and identifying these structures are shown in Figures 6(c) and (d). The density of G-phase precipitates around the Hf-rich particles was found to be noticeably lower than in regions away from the particles, and the extent of this low-density region scaled with the particle size.

A comparison of the microstructures of the gage section close to the fracture end of specimens H and L is shown in Figures 7(a) and (b), respectively. Specimen H, with a creep ductility of 12.3 pct, showed a uniform distribution of dislocations throughout the foil (Figure 7(a)). Extensive bypassing of the dislocations *via* Orowan looping was observed around the large G-phase precipitates, as clearly seen in the weak-beam dark-field (WBDF) images taken from this specimen (Figure 7(c)). In contrast, specimen L, which exhibited a creep ductility of ≈40 pct, showed very few dislocations in the matrix (Figure 7(b)). However, evidence

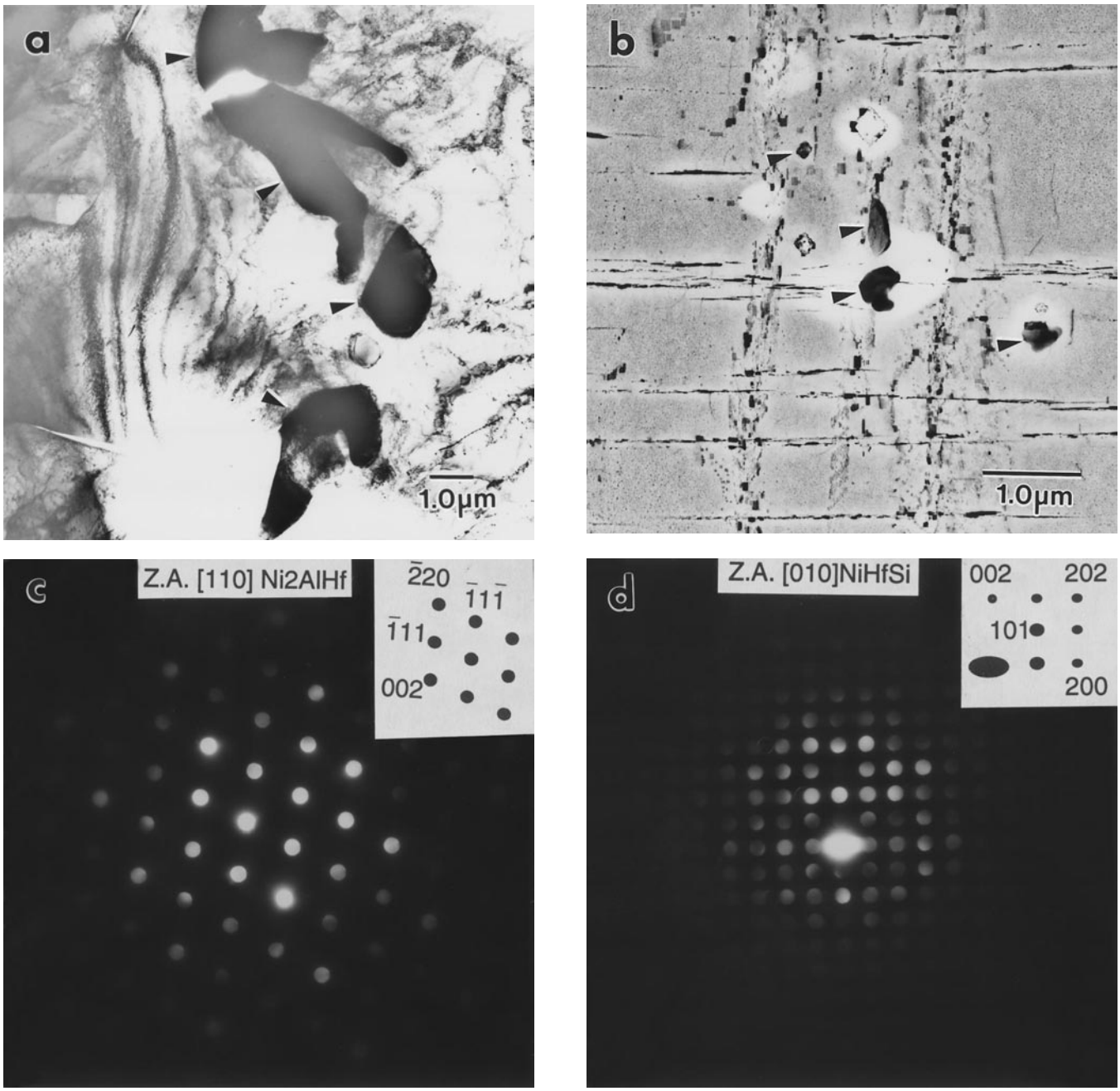

Fig. 6—Typical Hf-rich particles (arrowed) observed in the TEM foils made from the gage section of specimens (*a*) L and (*b*) H. (*c*) and (*d*) Selected MBED patterns identifying the Ni_2AlHf and NiHfSi phases, respectively.

for the formation of a number of shear bands in the microstructure was clearly seen in this specimen. A representative micrograph showing two of the shear bands marked by broken dark lines is shown in Figure 8, which is a bright-field image close to a ⟨010⟩ zone-axis and contains the stress axis. Assuming the stress axis to be [001] and the zone-axis to be [010], a trace analysis indicated that shear had occurred along the [101] direction. These observations are consistent with the macroscopic shear fracture that was exhibited by this sample and is shown in Figure 9. The presence of shear bands suggested that intense localized deformation had occurred in sample L. As a result of this shear deformation, subgrain formation was observed within the shear bands. These subgrains were mostly confined within the precipitate-free zones of the aligned G platelets, where dynamic recovery is expected to occur relatively easily due to a minimal dislocation-particle interaction. Some of these subgrains exhibiting a darker contrast are shown by arrows in Figure 8. No shear band formation or any such features were observed in sample H.

The microstructure of the gage section away from the fracture end exhibited a uniform distribution of dislocations in specimen H similar to that observed in the section close to the fracture surface (*e.g.*, Figure 7(a)). This suggested that the high-life specimen had deformed uniformly throughout the gage section. In contrast, the gage region away from the fracture end in specimen L showed very few dislocations and no evidence of deformation bands, thereby

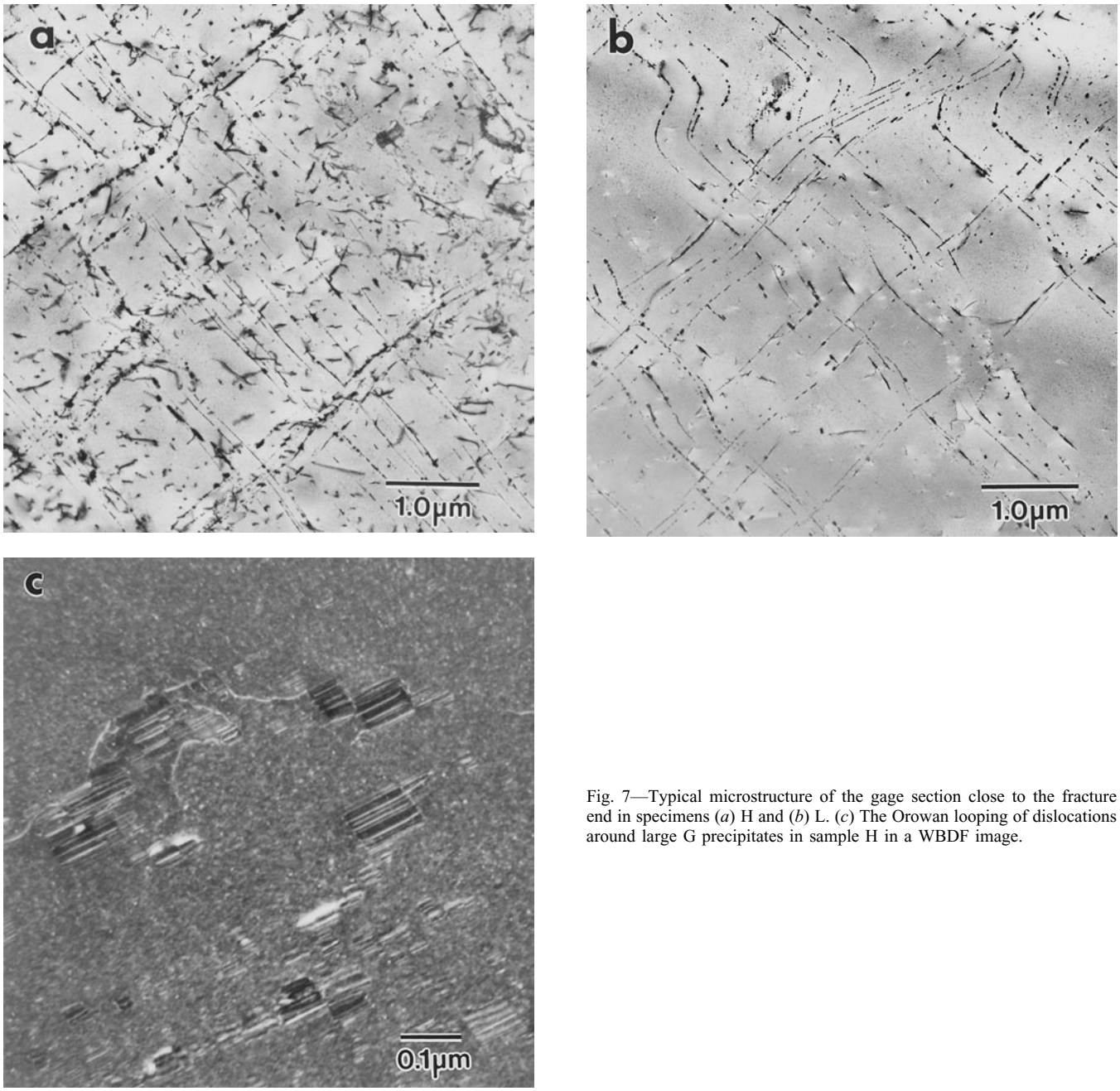

Fig. 7—Typical microstructure of the gage section close to the fracture end in specimens (*a*) H and (*b*) L. (*c*) The Orowan looping of dislocations around large G precipitates in sample H in a WBDF image.

suggesting that deformation in the low-life specimen was nonuniform and confined to regions close to where the fracture had occurred.

The TEM observations indicating a general lack of dislocations in specimen L after ≈40 pct strain were quite surprising. Although the G-phase microstructures of specimens L and H were very similar, a major difference observed between the two specimens was a noticeably higher density of large (>1.0 μm in size) Hf-rich particles in sample L. Therefore, it was decided to examine the regions adjacent to these particles in specimen L to see if they had played a role in altering the deformation behavior. Hf-rich particles were generally observed in relatively thicker sections of the foil. Nevertheless, careful and detailed observations revealed that the microstructure around these particles was very different from that observed in regions away from the particles. Figure 10(a) shows the microstructure around an Hf-rich particle which was present near the fracture end of specimen L. This particle had fallen out of the foil during electropolishing, leaving a hole (P) in its place. Comparing this region with the region observed away from the particle (*e.g.*, Figure 7(b)), it can be seen that the two regions are vastly different and that a large amount of deformation is locally confined around the Hf-rich particles. Figure 10(b) is a high-magnification view of region A in Figure 10(a), showing a clear view of the dislocation substructure. A large number of well-developed subgrain boundaries (arrowed) and dislocation networks are observed, thereby suggesting that intense deformation and dynamic recovery had occurred in regions around the Hf-rich particles. This was typical of the microstructures around all the large Hf-rich particles that were observed in

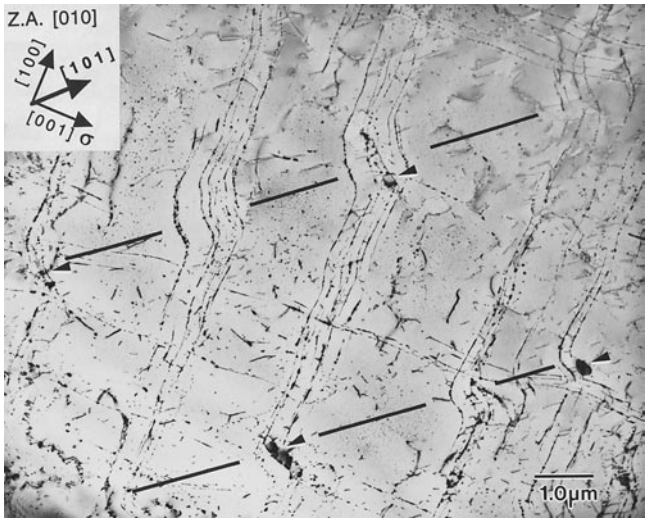

Fig. 8—Typical shear bands observed in specimen L near the fracture end.

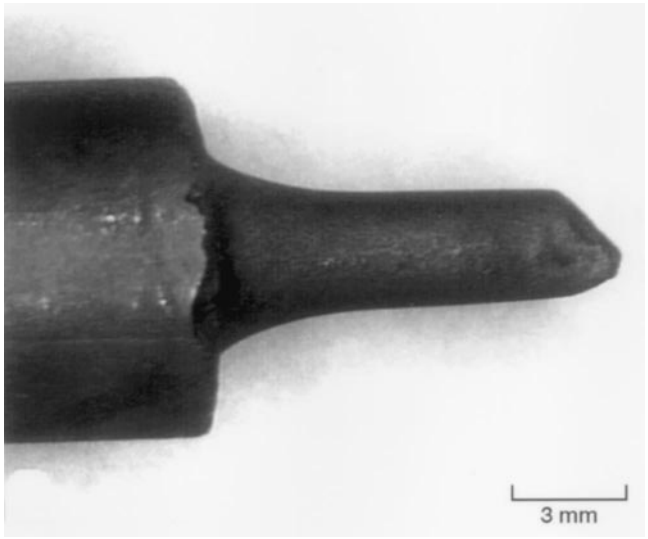

Fig. 9—Optical micrograph showing the macroscopic shear failure of specimen L.

sample L. This result is in absolute contrast to regions away from the particles where the density of dislocations was quite low (*e.g.*, Figure 7(b)). It is clear from these observations that the low-life sample had deformed nonuniformly, with intense localized deformation confined mostly around the Hf-rich particles.

The Burger's vectors of the dislocation networks observed in the vicinity of Hf-rich interdendritic particles were analyzed through diffraction contrast analysis. It was found that the networks consisted of $\mathbf{b} = \langle 100 \rangle$ dislocations. Such networks are thought to result from the decomposition of $\langle 101 \rangle$ deformation dislocations and were first observed and analyzed by Forbes *et al.*[13] in hard-oriented single crystals of NiAl after high-temperature deformation. The spacing of the networks was used to calculate the misorientation of the subgrains in the highly deformed regions some distance from the particles and it was found to be ≤4 deg. However, in regions close to the particle-matrix interface where distinct subgrain formation was observed (*e.g.*, region B in Figure 10(c)), overlapping SADPs indicated that the misorientations between these subgrains were as high as 14 deg (Figure 10(d)). These observations suggest that the large Hf-rich interdendritic particles had played an important role in influencing the creep and, hence, the rupture life. The smaller Hf-rich particles (≤1.0 μm in size) typically observed in sample H, however, did not show such an intense strain localization behavior. It is pertinent to mention that in a thicker section of the foil in specimen L where the particles were present and still intact, several slip bands were found to emanate from the Hf-rich particles (arrows in Figure 11). However, within the limits of subgrain misorientation observed around the Hf-rich particles, all the bands were almost parallel to each other and traces of any other slip system, either orthogonal or inclined, were not observed under any diffraction condition.

IV. DISCUSSION

Precipitate-strengthened crystals are prone to strain localization and shear band formation, especially when the precipitates are coherent and help concentrate the slip onto relatively few slip planes.[1] The G phase–strengthened NiAl-0.5Hf alloy examined in this study falls in this category. However, the SEM/TEM microstructural examination of the two specimens presented no evidence which would suggest that the fine coherent G-phase precipitates were in any way responsible for causing a shear failure in sample L. This is also reasonably justified in view of the fact that the two samples, in general, had very similar G-phase distributions. On the other hand, the microstructural study clearly indicated that a substantial difference in the size and density of Hf-rich interdendritic particles existed between the two samples, which was largely responsible for the observed change in the deformation behavior.

In a $\langle 001 \rangle$ crystal orientation, corresponding to the symmetry of the tensile axis, there exist four equivalent $\langle 011 \rangle$ slip directions which are arranged symmetrically to the axis at an angle of ± 45 deg. The accompanying slip systems with maximum resolved shear stress are $(10\bar{1})[101]$, $(101)[10\bar{1}]$, $(01\bar{1})[011]$, and $(011)[01\bar{1}]$ for the [001] orientation.[13,14] The SEM observations of a circular cross section along the sample length (Figure 1(a)), evidence of duplex slip traces on the specimen surface (Figure 1(c)), and TEM observations of a uniform dislocation distribution throughout the gage section (Figure 7(a)), suggest that the high-life sample had deformed uniformly by the activation of at least two orthogonal slip systems. In contrast, SEM observations of an elliptical fracture cross section (Figure 1(b)) and TEM observations of a generally low dislocation density in regions away from the fracture end (Figure 7(b)), coupled with the formation of shear bands close to the fracture surface (Figure 8), suggest that the low-life sample had deformed nonuniformly by, predominantly, a single slip mechanism. These observations suggest that this deviation from the expected multiple slip to a localized single slip behavior was likely responsible for lowering the creep rupture life.

The microprocess behind this plastic instability and, in particular, the strain softening mechanism which led to slip localization and macroscopic shear in sample L still need to be addressed. The major difference observed between the

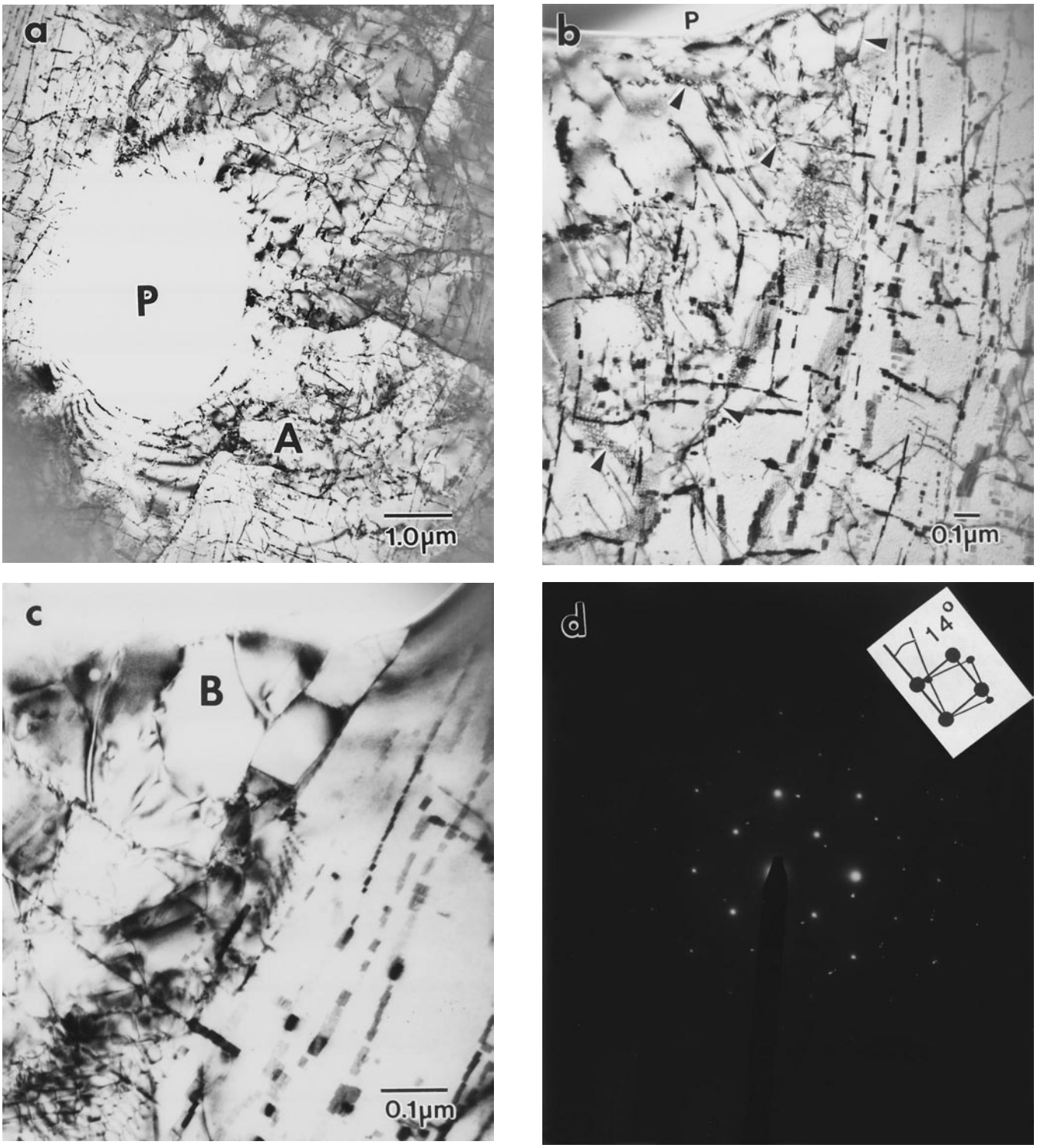

Fig. 10—TEM micrographs showing (*a*) intense localized plastic deformation around an etched-out Hf-rich particle (P) in specimen L. (*b*) Details of the substructure in region A of (a). (*c*) Distinct subgrain formation close to the particle-matrix interface. (*d*) SADP of region B in (c) showing a misorientation of 14 deg between the subgrains.

two samples was the noticeably higher density of large (>1.0 μm in size) Hf-rich particles in the low-life sample. The potent role of these particles in changing the deformation process or causing fracture can be rationalized in two ways. First, the large Hf-rich particles can be responsible for crack initiation and final failure in the material. However, keeping in mind that the strain to failure in sample L was ≈40 pct and the test temperature (1144 K) was above the brittle-to-ductile transition temperature,[14] this, in general, is not expected. Even if cracks originate at these particles, the plasticity exhibited by the matrix is expected to be high enough to prevent their catastrophic propagation to final fracture.

A second way by which the Hf-rich particles can affect

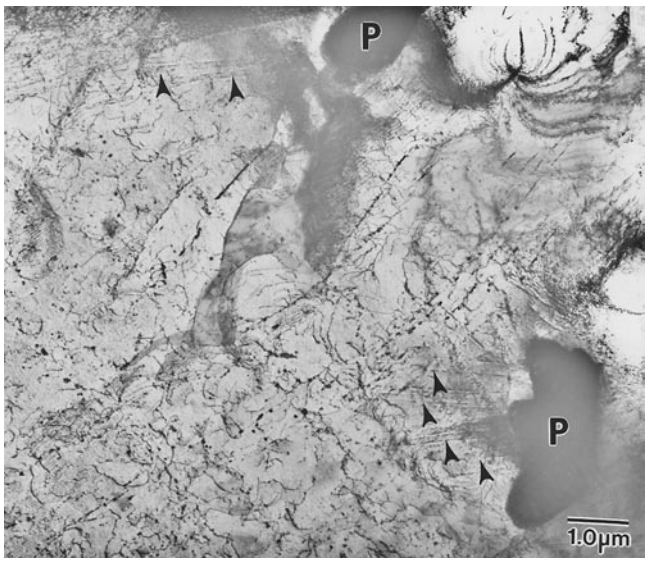

Fig. 11—A TEM micrograph showing emission of slip bands (arrowed) from two Hf-rich particles, marked P, in specimen L.

the deformation behavior is to influence the plasticity of the matrix. In a precipitate-hardened alloy, strength is strongly dependent on the size and interparticle spacing of the second-phase particles. The presence of Hf-rich particles depletes the surrounding matrix of Hf and Si (Figure 4), thereby leading to a lower density of the G-phase precipitates in their immediate vicinity. Since this decrease in precipitate density corresponds to an increase in the G-precipitate spacing, the regions around the Hf-rich particles are expected to be of lower strength than the rest of the matrix. This creates localized ''soft'' regions around the particles which can deform more easily than the rest of the matrix. The volume of soft region varies in direct proportion to the size of the particle; the bigger the Hf-rich particle, the greater the extent of solute depletion and the larger the volume of soft region. The smaller Hf-rich particles do not produce such large heterogeneity in the microstructure, as they have small soft regions associated with them. In addition to producing soft regions, the larger particles can also generate large stress gradients in the material. Finite element simulations have shown that under the action of an applied stress, the average von Mises stress distribution in a matrix with a reinforced particle changes considerably, especially around and near the particle.[15] In the presence of a large number of particles with a range of sizes and arbitrary shapes, the stress distribution is quite complex and is a function of several factors such as the particle aspect ratio, particle volume fraction, and their orientation relative to the loading axis and with respect to each other.[15] Based on the results of these simulations, it is reasonable to assume that if large Hf-rich particles are present in a specimen they can play an important role in changing the local stress distribution, which would have been otherwise quite uniform. In turn, the localized stress concentrations that develop near the particles, along with the fact that these particles are potential sites for nucleation of dislocations, can promote strong localized plastic deformation.[16] The soft regions produced by a lower density of G-phase precipitates around the particles also help to accentuate this localized deformation. Recovery and recrystallization processes occurring in the soft regions can then produce large lattice rotations, which in turn result in local geometrical softening favoring one slip system over the other, as observed in Figure 11. In the presence of a large number of such particles, a co-ordinated propagation of the microscopically localized slip can eventually develop into a shear zone which can penetrate the entire sample cross section, causing failure.

As noted in the experimental section, the low- and high-life samples were machined from two different ingots. The presence of undissolved interdendritic Hf-rich particles in one ingot (*e.g.*, sample L) *vs* another (*e.g.*, sample H) suggests that NiAl-Hf alloys are sensitive to inherent changes in the processing and heat-treatment conditions. Both a variation in the amount of as-cast interdendritic structure due to a different extent of reaction between the melt and mold in different ingots, and a slight variation in the furnace temperature in the batch homogenization process are likely to contribute toward incomplete homogenization of the various interdendritic intermetallic phases. Thus, these results clearly suggest that optimization, modification, and proper control of casting and homogenization conditions to minimize the size and density of these Hf-rich particles are very important in order to avoid premature failure in the creep rupture life of NiAl-Hf single-crystal alloys.

V. SUMMARY AND CONCLUSIONS

The present study has demonstrated that the presence of large (>1.0 μm in size) undissolved Hf-rich interdendritic particles can have a detrimental effect on the creep life of NiAl-Hf single-crystal alloys. This effect is accentuated for two reasons. First, these large particles deplete the surrounding matrix of Hf and Si, which in turn leads to a lower density of G phase, thereby producing soft regions around the particles. Second, the presence of these particles sets up a nonuniform stress distribution in the material. Both of these effects result in localized deformation which, in turn, could cause plastic instability in the material, thereby leading to a change in the deformation mode from multiple to a single slip. The net result of this change in the deformation mode is the reduction in the stress rupture lives of the NiAl-Hf single crystals.

ACKNOWLEDGMENTS

The authors acknowledge fruitful discussions on plastic instability and shear failure with Professor John Hirth, Washington State University, Pullman. Special thanks to Dr. R. Mackay, NASA–Lewis Research Center for reviewing the article. Help from several of our colleagues during various stages of this study is also gratefully acknowledged.

REFERENCES

1. A. Luft: *Prog. Mater. Sci.*, 1991, vol. 35, pp. 140-45.
2. R.D. Noebe, R.R. Bowman, and M.V. Nathal: *Int. Mater. Rev.*, 1993, vol. 38, pp. 193-232.
3. R. Darolia, D.F. Lahrman, R.D. Field, J.R. Dobbs, K.M. Chang, E.H. Goldman, and D.G. Konitzer: *Ordered Intermetallics—Physical Metallurgy and Mechanical Behavior*, Kluwer Academic Publishers, Dordrecht, The Netherlands, 1992, pp. 679-98.
4. R. Darolia: *JOM*, 1991, pp. 44-49.

5. R. Darolia: in *Structural Intermetallics*, R. Darolia, J.J. Lewandowski, C.T. Liu, P.L. Martin, D.B. Miracle, and M.V. Nathal, eds., TMS, Warrendale, PA, 1993, pp. 495-504.
6. W.S. Walston, R.D. Field, J.R. Dobbs, D.F. Lahrman, and R. Darolia: in *Structural Intermetallics*, R. Darolia, J.J. Lewandowski, C.T. Liu, P.L. Martin, D.B. Miracle, and M.V. Nathal, eds., TMS, Warrendale, PA, 1993, pp. 523-32.
7. I.E. Locci, R.D. Noebe, R.R. Bowman, R.V. Miner, M.V. Nathal, and R. Darolia: in *High-Temperature Ordered Intermetallics Alloys IV*, L. Johnson, D.P. Pope, and J.O. Stiegler, eds., Materials Research Society, Pittsburgh, PA, 1991, pp. 1013-18.
8. A. Garg, S.V. Raj, and R. Darolia: in *Micromechanisms of Advanced Materials*, S.N.G. Chu, P.K. Liaw, R.J. Arsenault, K. Sadananda, K.S. Chan, W.W. Gerberich, C.C. Chau, and T.M. Kung, TMS, Warrendale, PA, 1995, pp. 255-63.
9. R.D. Noebe, P.O. Dickerson, and A. Garg: NASA Technical Memorandum 107029, NASA, Washington, DC, 1995, pp. 1-29.
10. A. Garg, R.D. Noebe, and R. Darolia: *Proc. Annual HITEMP Review—1995*, NASA–Lewis Research Center, Cleveland, OH, 1995, vol. II, pp. 1-12.
11. I.E. Locci, R.M. Dickerson, A. Garg, R.D. Noebe, J.D. Whittenberger, M.V. Nathal, and R. Darolia: *J. Mater. Res.*, 1996, vol. 11, (12), pp. 3024-38.
12. A. Garg, R.D. Noebe, and R. Darolia: *Acta Mater.*, 1996, vol. 44, (7), pp. 2809-20.
13. K.R. Forbes, U. Glatzel, R. Darolia, and W.D. Nix: in *High-Temperature Ordered Intermetallics Alloys V*, I. Baker, R. Darolia, J.D. Whittenberger, and M.H. Yoo, eds., Materials Research Society, Pittsburgh, PA, 1993, vol. 288, pp. 45-57.
14. R. Darolia, R.D. Field, R.D. Noebe, A. Garg, and W.S. Walston: AFOSR Contract Report No. GEAE/F49620-91-C-0077, GE Aircraft Engines, Cincinnati, OH, 1995, pp. 1-195.
15. Z. Wang, T.K. Chen, and D.J. Lloyd: *Metall. Trans. A*, 1993, vol. 24A, pp. 197-207.
16. J.G. Cowie and F.R. Tuler: *Mater. Sci. Eng.*, 1987, vol. 95, pp. 93-99.